Handheld optofluidic platform towards binding dynamics applications in field-settings

Sena Yaman [a,b,1], Meryem Beyza Avci [a,c,1], Fatma Kurul [a,d], Seda Nur Topkaya [e], Arif E. Cetin [a,*]

[a] Izmir Biomedicine and Genome Center, Balcova, Izmir 35340, Turkey
[b] Department of Radiology, Stanford University, Palo Alto, CA 94304, USA
[c] Department of Electrical and Electronics Engineering, Izmir University of Economics, Balcova, Izmir 35330, Turkey
[d] Izmir International Biomedicine and Genome Institute, Dokuz Eylul University, Balcova, Izmir 35340, Turkey
[e] Department of Analytical Chemistry, Faculty of Pharmacy, Izmir Katip Celebi University, Cigli, Izmir 35620, Turkey

ARTICLE INFO

ABSTRACT

We have introduced a lensfree optofluidic platform that incorporates subwavelength nanohole arrays, a compact microfluidics system, and on-chip computational imaging to enable label-free identification of biomolecular interactions. Our platform weighs only 260 g and has dimensions of 16 cm × 10 cm × 11 cm. It utilizes a CMOS imager to capture plasmonic diffraction field images, offering a wide field-of-view of up to 11.5 mm^2 for refractive index sensing. To illuminate the plasmonic chip, we employ an LED source positioned close to the transmission resonance of the nanohole arrays. This LED source creates diffraction patterns on the imager. The platform ensures the targeted delivery of analytes to the ligand-coated sensing surface using microfluidics. By analyzing real-time variations within the diffraction field images, we could reveal the time-dependent binding dynamics of biomolecules. Our platform has demonstrated an experimentally obtained limit of detection (LOD) as low as 5 ng/mL for protein IgG. Furthermore, based on the real-time diffraction field images, we successfully determine the association and disassociation constants, which account for the binding and detachment between protein A/G and IgG. We have also developed a software that allows full control of the hardware settings of the portable platform, including the camera and pump system. This software also incorporates an image-processing algorithm to calculate the binding parameters for the analytes of interest. Providing high-quality sensing capabilities in a cost-effective infrastructure, we believe that our optofluidic biosensor platform offers significant advantages for surface plasmon resonance (SPR) applications for field-settings.

1. Introduction

Compact and portable biosensing technologies are crucial for replacing classical counterparts that require bulky and expensive equipment and sophisticated infrastructure. By employing these easy-to-use and low-cost devices, biosensing tests could be conducted in resource-poor settings, accelerating the decentralization of applications reliant on biosensors [1,2]. One important biosensing approach is the use of optics, which could be either in labeled or label-free format [3]. Biosensors utilizing optical labels, e.g., fluorescent dyes, are widely used to detect analytes such as proteins, nucleic acids, or pathogens.[4] However, fluorescence labeling has several drawbacks, including expensive and complex sample preparation protocols, the risk of

mismatch between the number of fluorophores and the targeted analyte, and photo-bleaching [5]. To address these limitations in optical labeling, label-free techniques are widely preferred as they eliminate the need for fluorescent dyes by utilizing sensing-by-binding approaches.[6, 7] Ideally, label-free biosensors allow for the simultaneous identification of multiple analytes, enabling multiplexed and high-throughput applications. Various label-free sensing techniques have been introduced to meet this demand, including photonic crystals,[8] optical micro-cavities,[9] surface plasmon resonance (SPR),[10] and nano-textured metal films [11]. Among these, subwavelength nanoholes offer significant advantages as they combine the strong properties of propagating and localized surface plasmons in the far- and near-field regions [12]. Metallic nanohole arrays, capable of confining light at the nanometer

* Corresponding author.
 E-mail address: arifengin.cetin@ibg.edu.tr (A.E. Cetin).
 [1] These authors contributed equally to this work.

scale with large electromagnetic field intensities, exhibit high refractive index sensitivities, making them highly promising for biodetection applications.[13] In contrast to classical commercial SPR platforms that rely on flat metal films, nanohole arrays with their periodic lattice geometry enable surface plasmon excitation even under normally incident light sources, simplifying optical alignment by eliminating angular illumination sensitivity. This collinear configuration is crucial for realizing field-deployable biosensor platforms for point-of-care applications in resource-poor settings [14]. By monitoring plasmonic excitations through extraordinary light transmission phenomena, plasmonic substrates based on nanohole arrays enable signal evaluation in an array format using an imager instead of a spectrometer or photodetector, facilitating the multi-detection of analytes on the same plasmonic chip surface with high signal-to-noise ratio [15].

Despite their unique optical properties that provide strong sensitivity for biosensing applications, techniques relying on these plasmonic nanohole arrays require the use of benchtop read-out instrumentation, which increases costs and limits their use in field settings. Thus, there is a need for field-deployable biosensors that could allow high-throughput biosensing without the need for optical labels [16,17]. In this regard, we recently introduced a handheld and lens-free plasmonic biosensor that integrates plasmonic nanohole arrays and computational on-chip imaging to detect ultrathin layers of protein complexes [18]. We successfully employed this technology for virus detection, demonstrating its potential use for disease diagnosis in field settings [19]. By integrating this plasmonic read-out scheme with a microfluidic chamber and an external bulky syringe pump setup, we could monitor in real-time the simultaneous binding events between protein molecules on the surface of a plasmonic chip composed of periodic nanoholes [20].

In this paper, we take a significant stride towards advancing the application of our handheld biosensor technology for commercial surface plasmon resonance (SPR) applications. Our innovative approach combines the plasmonic read-out scheme with a compact microfluidic framework on a single portable platform, pushing the boundaries of this technology. By integrating the plasmonic substrate into a microfluidic chamber, we enable the binding of analytes on the plasmonic surface while maintaining precise control over the flow through a custom-made pump setting. Notably, we introduce a straightforward, low-cost, and cleanroom-free manufacturing technique to realize the microfluidic chamber, underscoring the practicality and accessibility of our approach. To delve deeper into the binding mechanisms between analytes, we harness the power of both a CMOS camera and the pump simultaneously, capturing real-time plasmonic images. This synergistic combination empowers us to unravel the intricate details of the analyte interactions. Furthermore, we employ a cost-effective and high-throughput nanofabrication technique to fabricate nanohole arrays, enhancing the performance and scalability of our handheld platform. Notably, we depart from our previous versions, which relied on commercial programming languages for biosensing information extraction or separate control of external devices using proprietary software. Instead, we have developed our own software that efficiently operates all the constituent hardware components of the lens-free platform. This comprehensive software not only facilitates functionality but also processes plasmonic diffraction field images to provide valuable sensing information. With these advancements, our handheld biosensor technology stands as a significant leap forward, opening new possibilities for rapid and field-deployable biosensing applications in various domains.

2. Optofluidic plasmonic biosensor platform

Fig. 1A and 1B depict the schematics and photograph of the optofluidic plasmonic platform, respectively. To facilitate the acquisition of high-quality diffraction field images by minimizing background noise and consolidating all hardware components, we fabricated a case using filament-based 3D-printing technology. This box provides a dark environment for optimal imaging conditions. The platform comprises four main components: (i) Plasmonic Chip, (ii) Imaging Module, (iii) Microfluidic Module, and (iv) Software Module. The Plasmonic Chip consists of a thin gold film embedded with periodic nanohole arrays. In the Imaging Module, a red LED (light-emitting-diode) source illuminates the plasmonic chip, while a CMOS camera (Complementary Metal Oxide Semiconductor) captures the transmitted light, enabling the recording of diffraction field patterns produced by the plasmonic nanoholes. The Microfluidic Module incorporates a one-channel polydimethylsiloxane (PDMS)-based microfluidic chamber and a micro-controller-driven piezo-pump system. This module facilitates precise delivery of analytes to the sensing surface, which is functionalized with capturing ligands, allowing real-time monitoring of binding events (as shown in Fig. 1C). The Software Module consists of a user-friendly graphical user interface (GUI) that facilitates simultaneous control of the optical and microfluidic components. Additionally, it incorporates an image-processing algorithm that utilizes real-time plasmonic diffraction field images to determine the relevant binding parameters. System control and feeding could be achieved via either a notebook or single board computer, where the communication between Imaging Module and Microfluidic Module are realized through USB (universal serial bus).
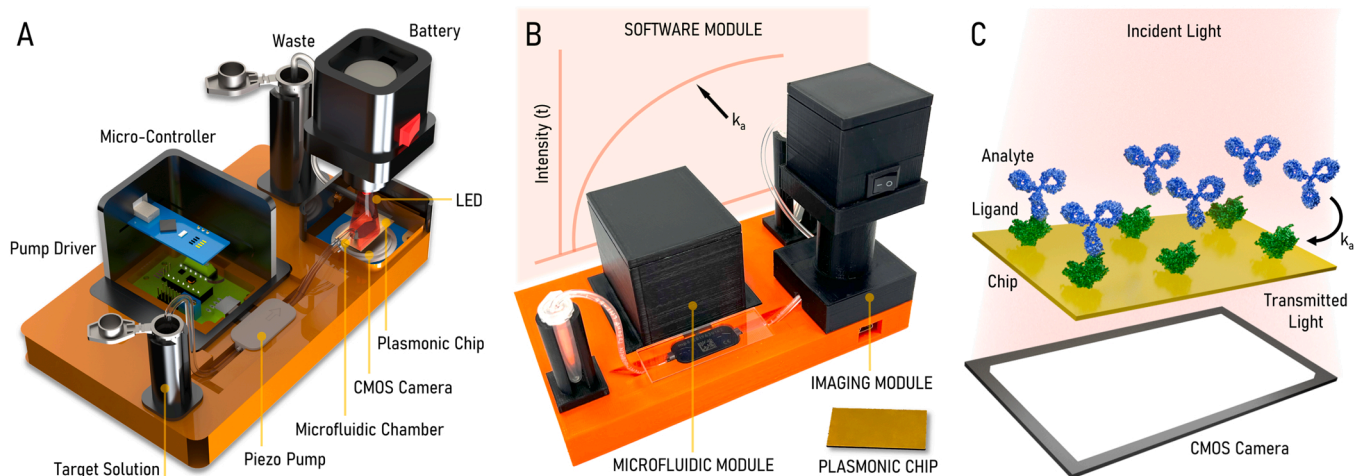
Fig. 1. (A) Schematics and (B) photograph of the portable plasmonic platform designed for assessing real-time biomolecular interactions in field-settings. (C) Schematics illustrating the targeted delivery of analytes onto the ligand-immobilized surface of the plasmonic chip, leading to variations in the intensity of the recorded diffraction field images under LED illumination, as captured by a CMOS camera.

3. Plasmonic chip

The plasmonic chip is constructed with subwavelength nanohole arrays fabricated on a 120 nm gold film. The nanoholes were intentionally designed to have a diameter of 150 nm, and the array was created with a periodicity of 450 nm. This choice of dimensions ensures that the transmission resonance supported by the nanohole arrays aligns spectrally with the LED source. Furthermore, the selection of these specific geometrical parameters aimed to induce a plasmonic resonance within an elevated wavelength range, as modes at longer wavelengths exhibit higher refractive index sensitivities [21]. This choice was made while considering the wavelength range corresponding to the optimal quantum efficiency of the CMOS camera. The supporting substrate beneath the gold film is made of fused silica (glass) coated with a 100 nm silicon nitride film (SiN). This thin SiN interlayer serves as a high refractive index material, effectively eliminating undesired plasmonic modes between the gold film and fused the silica substrate. It enables an isolated and well-defined plasmonic resonance within the desired spectral region [22]. Fig. 2A illustrates the optical response of the nanohole arrays in phosphate-buffered saline (PBS) medium, demonstrating a transmission resonance occurring at ~665.1 nm. This resonance arises from surface plasmon excitations at the top surface of the gold film along the interface between the PBS medium and the gold film, specifically the Au/Med(1,0) mode. To investigate the origin of this transmission resonance, finite-difference time-domain (FDTD) simulations were conducted. The simulation employed periodic boundary conditions along the xy-plane to replicate array behavior, while a perfectly matched layer was utilized along the propagation direction (z-axis). Refractive index data for the materials comprising the plasmonic chip was obtained from [23]. Nearfield calculations of the magnetic field reveal the modality of the transmission resonance, which combines both localized and propagating surface plasmons (Fig. 2A inset). When illuminated with an x-polarized light source, the magnetic field distribution associated with this mode exhibits two symmetric standing field patterns along the x-axis, indicating the presence of two counter-propagating surface plasmons. Additionally, two hot spots at the aperture rims arise from the localized surface plasmons along the y-axis. The electric field distribution (Fig. 2B - left) confirms the dipolar nature of the mode, with intense field enhancements localized around the nanohole rims along the x-axis. These local fields, concentrated around the top gold surface rims, extend into the surrounding medium (Fig. 2B - right), making them accessible to analytes captured on the gold sensing surface. Notably, due to the circular shape of the subwavelength nanoholes, which exhibits symmetry in all directions, an unpolarized LED source was employed in the imaging module. This configuration ensures that local fields are concentrated uniformly along the rims, resulting in stronger sensitivities compared to those achieved with a polarized incident field.

The choice of the fabrication method depends on the specific requirements of the plasmonic device. To ensure reliable sensing data, a robust imaging technique is needed, which could be achieved with plasmonic diffraction fields uniformly distributed over a large area. To address this requirement, we employed a high-throughput fabrication method suitable for high-resolution and large-area fabrication using deep ultraviolet (UV) lithography (Fig. 2C). The fabrication process was carried out on a 4-inch fused silica wafer coated with a 100 nm LPCVD (low-pressure chemical vapor deposition) silicon nitride film. Firstly, we deposited a 120 nm gold layer on the silicon nitride interlayer, utilizing a 5 nm chromium (Cr) adhesion layer. The gold surface was then coated with a resist, and subjected to deep UV lithography. After development, dry etching was performed using a mixture of sulfur hexafluoride (SF_6) and argon (Ar) to create apertures through the resist and gold film. The
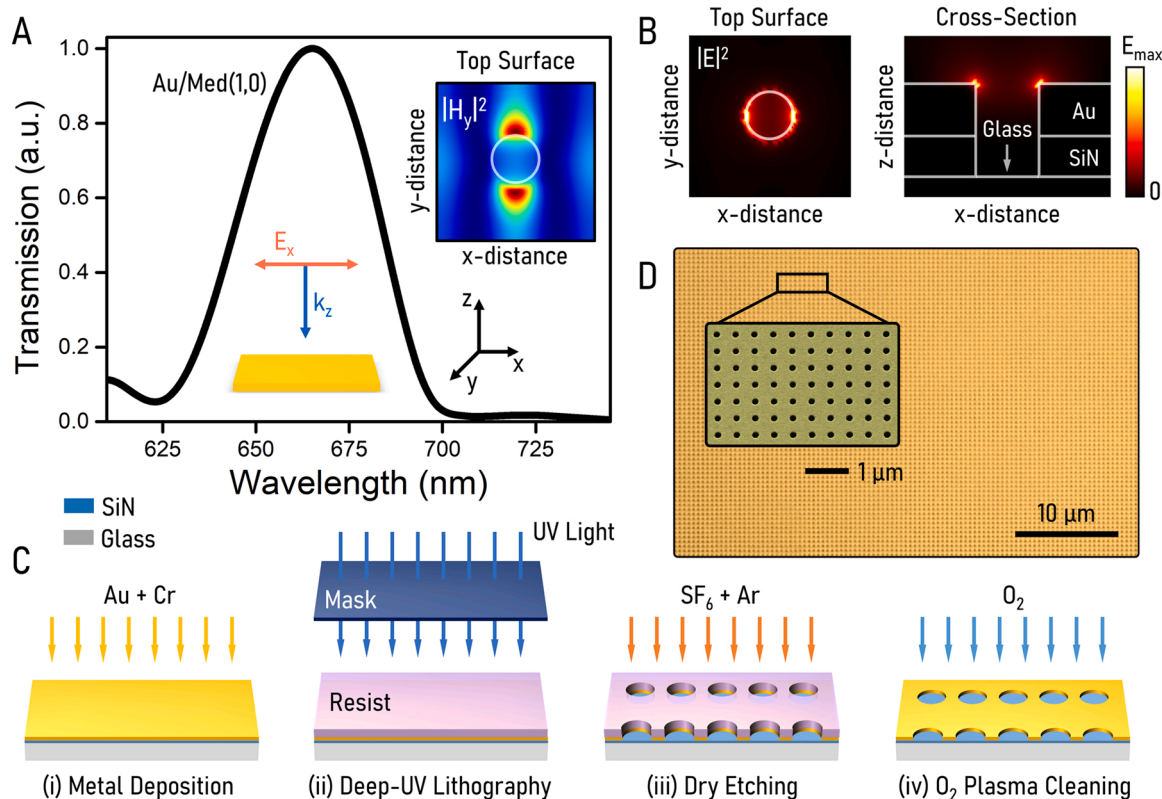
Fig. 2. (A) Transmission spectrum of the nano hole arrays. Inset: The y-component of the magnetic field intensity calculated at the top surface of the gold film under an x-polarized light source. The inset also shows the polarization and propagation directions of the incident light source. (B) Electric field intensity calculated at the top surface of the gold film and its cross-sectional profile. (C) Steps of the high-throughput fabrication technique based on deep-UV lithography. (D) Bright-field microscopy image and SEM image of the plasmonic chip.

remaining resist was removed from the gold surface using oxygen (O₂) plasma. Finally, the wafer was diced to obtain 2×1 cm^2 plasmonic chips. This fabrication technique significantly increased throughput by allowing simultaneous production of multiple plasmonic chips on the same wafer, unlike classical techniques based on electron-beam lithography, where plasmonic chips with subwavelength features must be produced sequentially. In Fig. 2D, the bright-field microscopy image demonstrates well-defined and uniformly distributed subwavelength nanoholes over a millimeter scale, and the scanning electron microscopy (SEM) image confirms the quality of our fabrication. Although our fabrication method relies on a sophisticated and expensive infrastructure, such as a cleanroom, the high-throughput nature of our technique greatly reduces the cost of each chip to ~\$3. While there are other techniques available in the literature for realizing plasmonic structures, such as self-assembly techniques or chemical synthesis and deposition offer cost advantages, they have limitations in terms of resolution, replicability, scalability, or complexity of the plasmonic structures.

4. Imaging module

Fig. 3A depicts the imaging module of the portable platform, which includes an LED light source and a CMOS camera. The plasmonic chip is positioned directly in front of the camera, secured by a rectangular-shaped holder to ensure its stability during the real-time measurements. Our technology employs an imaging-based methodology to determine the real-time refractive index changes resulting from the increase in the biomass on the plasmonic chip surface. By utilizing the system software, the operator can select a specific area on the plasmonic

chip to monitor the diffracting field intensity images in real-time. This approach resembles the spectrometer-based read-out schemes that rely on spectral variations within the plasmonic resonances, which are calculated from a single location on the plasmonic chip surface. In Fig. 3B, the optical characteristics of these components are shown, along with the transmission spectrum of the plasmonic chip functionalized with protein mono- and bilayers under the PBS solution. Our technology relies on sensing-by-binding, where the accumulation of analytes on the sensing surface alters the effective refractive index of the adjacent medium, resulting in a shift of the transmission resonance towards longer wavelengths. In our platform, we monitor the variations in diffraction field intensity images to obtain spectral read-out. To induce diffraction field intensity changes upon analyte attachment, we utilize an LED source (Ushio Opto Semiconductors, Inc., L690–02 AU) positioned at a wavelength of approximately 691.4 nm (red curve), which is longer than the transmission resonance of the plasmonic chip when saturated with the target analytes. This ensures that the transmission resonance always lies at shorter wavelengths than the LED source, preserving the Lorentzian shape of the resonance and ensuring reliable sensing data. For our intensity-based sensing approach, we chose a monochromatic CMOS camera (Thorlabs Inc., DCC1545M) with a high quantum efficiency within the relevant spectral window (black curve). Using USAF 1951Resolution Target, we determined the spatial resolution of the system as ~140.25 µm per line pair. The image resolution is high enough for our imaging-based methodology, which allows us to create diffraction field intensity images and determine spectral variations resulting from changes in biomass on the sensor surface.

In order to illustrate the working principle of our imaging-based
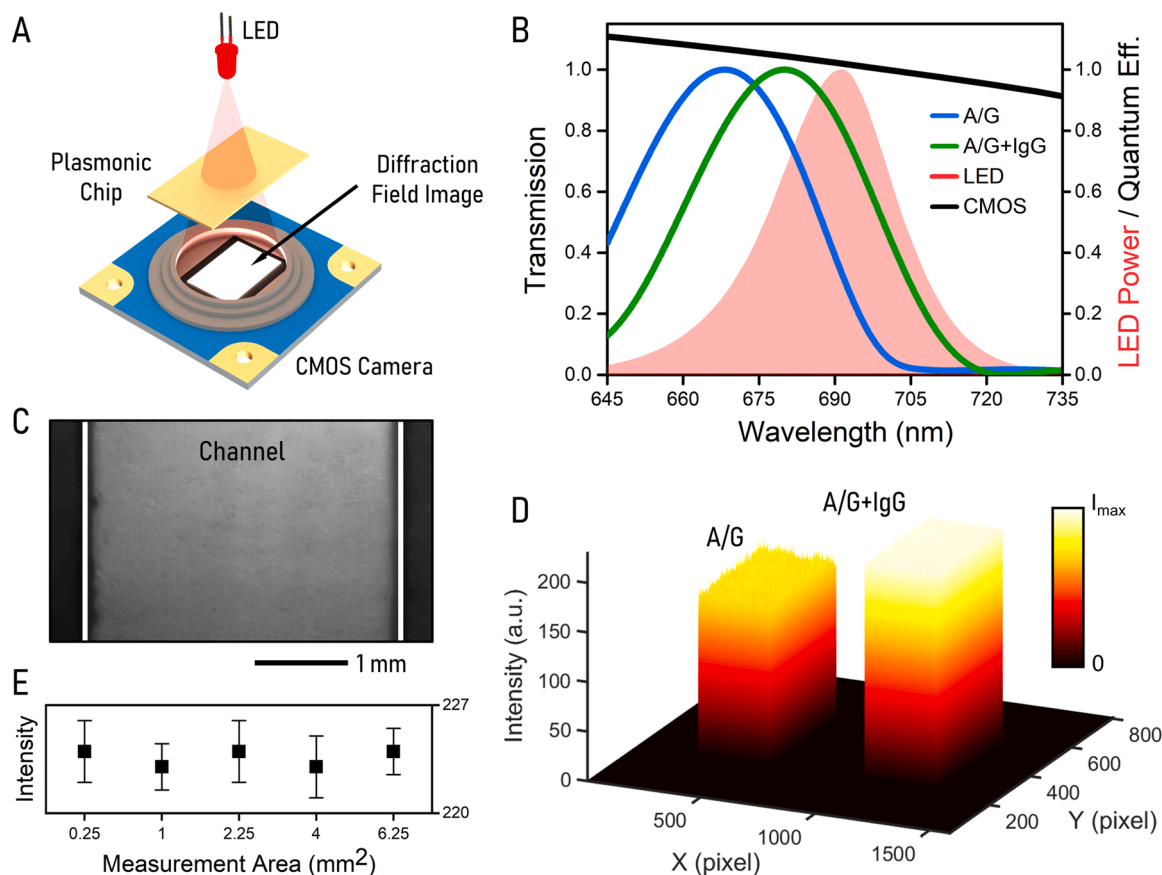
Fig. 3. (A) The imaging module of the portable plasmonic platform, comprising an LED light source and a CMOS camera. (B) Transmission resonance of the nanohole arrays functionalized with protein A/G (blue) and protein IgG (green) under PBS medium, along with the radiation power of the LED (red) and the quantum efficiency of the CMOS camera (black). (C) CMOS camera image of the plasmonic chip integrated into a one-channel microfluidic chamber containing PBS solution. (D) Three-dimensional visualization of the diffraction field intensities of the nanohole arrays functionalized with protein A/G and IgG. (E) Averaged diffraction field intensities calculated within various measurement areas on the same CMOS image of the plasmonic chip.

platform, we employed protein A/G (Thermo Fisher Scientific Inc.) as the ligand protein immobilized on the sensing surface and protein IgG (Sigma-Aldrich®) as the targeted analyte. Protein A/G is a recombinant fusion protein containing the binding domains of protein A and G [24]. Initially, the gold sensing surface was functionalized with protein A/G through physisorption, where the protein was simply pipetted on the chip surface, allowing for the attachment of protein IgG to form a strong protein bilayer through the Fc region. The transmission resonance, initially positioned at ~665.1 nm (Fig. 2A), shifted to ~668.2 nm (blue curve) and ~680 nm (green curve) after functionalizing the surface with 100 μg/mL protein A/G and 100 μg/mL protein IgG, respectively. All measurements were conducted in PBS medium. In Fig. 3C, the CMOS camera image of the plasmonic chip under PBS is presented, demonstrating the uniform diffraction field intensity across the 3.4 mm wide microfluidic channel. Fig. 3D presents the three-dimensional visualization of the diffraction field intensities corresponding to protein A/G and protein IgG attachments on the plasmonic chip surface. As anticipated, upon IgG immobilization, there is an additional spectral shift, effectively moving the transmission resonance towards longer wavelengths, aligning it more favorably with the LED response, resulting in a discernible increase in the diffraction field intensity compared to the case of protein A/G immobilization. The wide field-of-view of the camera, approximately 4.1 mm × 2.8 mm = ~11.5 mm^2, allows for monitoring binding events at multiple locations, which is crucial for obtaining reliable sensing data by simultaneously combining multiple spectral information using the diffraction field intensity changes [25]. Due to the homogeneous and uniformly distributed nanohole openings across the plasmonic chip surface, achieved through our precise and large-area fabrication method based on deep-UV lithography, our calculation method for determining spectral variations using diffraction field intensity images demonstrates remarkable robustness across various measurement areas on the CMOS images. As demonstrated later, we employ averaged diffraction field intensities for real-time binding kinetic analysis, where the operator selects the measurement area using our Software Module. For instance, Fig. 3E shows the averaged diffraction field intensities for different measurement areas on the same CMOS image, with the variation between each calculation, e.g., as low as 0.81%, proving the accuracy and reliability of our approach.

5. Microfluidic Module

The microfluidic module of the portable biosensor platform consists of two main components: (i) a one-channel PDMS-based microfluidic chamber, and (ii) a micro-controller driven piezo-pump system. To fabricate the microfluidic chamber, we used a mold created by CNC drilling on a 1.6 mm thick FR4 PCB plate coated with a thin copper film. Figs. 4B and 4C-top illustrate the schematic and photograph of the PCB mold, respectively. Fig. 4C-bottom shows the one-channel microfluidic chamber bonded to the plasmonic chip surface. The microfluidic channel has dimension of 6.7 mm × 3.4 mm, which is partly captured by the CMOS camera. Due to the CNC drilling marks on the PCB mold, the PDMS surface left an uneven surface that needed to be bonded to the plasmonic chip. Therefore, a thin layer of liquid PDMS was applied to the PDMS surface instead of using plasma activation. The PDMS layer was then placed on the plasmonic chip surface, and cured at 70 °C to ensure secure bonding (Fig. 4C-bottom). For connecting the tubing to the microfluidic chamber's inlet and outlet, two connectors were fabricated using resin-based 3D-printing. A leak-free flow could be ensured by using an apparatus that sandwiches the plasmonic chip inside. However, this requires a supporting cap underneath, which increases the distance between the plasmonic chip and the active area of the CMOS imager. In the presence of a lens-free methodology, this additional distance leads to the overlapping of diffraction patterns, potentially reducing the accuracy of intensity-based image processing. On the other hand, integrating the PDMS layer on the surface of the plasmonic chip (Fig. 4C), allows us to directly position the plasmonic
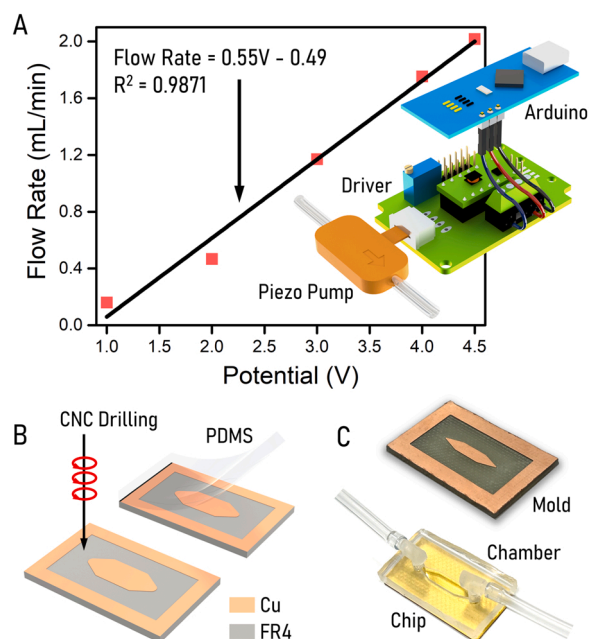
Fig. 4. (A) Flow rate of the piezo pump vs. the potential applied to the pump. A linear regression was fitted (black line) to the experimental data (red squares). The figure inset shows a schematic illustration of the circuit scheme for the micro-controller-driven piezo pump system. (B) Fabrication process of the PDMS microfluidic chip using CNC drilling. (C) Photographs of the PCB mold and the PDMS-based microfluidic chamber bonded to the plasmonic chip surface.

chip on top of the CMOS camera using a 3D-printed thin holder as schematically illustrated in Fig. 1A. This ensures the minimum distance between the plasmonic chip and the CMOS imager.

As depicted in Fig. 4A-inset, the piezo-pump system comprises a piezoelectric pump (Bartels Mikrotechnik GmbH, mp6-liq), a driver board, and a micro-controller (Arduino® Nano). The micro-controller-based driver board enables adjustment of the flow rates by varying the supply voltage of the piezoelectric pump within the range of 1.0–4.5 V. The micro-controller utilizes pulse-width modulation (PWM) to generate variable-width pulses that represent the amplitude of an analog signal used as input for the driver board. The frequency of the piezo-electric pump was maintained at 100 Hz to ensure that the linear relationship between voltage and flow rate remained unaffected by frequency. The PWM signal obtained from the micro-controller was amplified by the driver board to operate the piezoelectric pump. To establish the correlation between input voltage and flow rate, calibration tests were conducted using DI-water. The flow rate was measured for five different voltages applied over a period of 60 s. DI-water was chosen for the calibration tests due to its density of 1 kg/m^3, which allowed calculation of the flow rate based on the mass and density of the solution. The mass of DI-water dispensed by the pump in a specific duration was determined using a precision balance. The flow rate (mL/min) of the piezo pumps was calculated using the formula, *Flow Rate = Mass × Density × Time*(min). In Fig. 4A, it could be observed that the flow rate increases with the supply voltage, and a linear regression (black line) was fitted to the experimental data (red squares). The flow rate used for real-time binding experiments was set to 150 μL/min, which necessitates a total analyte solution volume of 2.25 mL.

6. Limit-of-detection of the optofluidic plasmonic platform

To determine the minimum analyte concentration detectable with our portable plasmonic platform (limit of detection: LOD), we conducted calibration tests using protein mono- and bilayers. Firstly, the plasmonic

chip surface was functionalized with 100 µg/mL protein A/G. Subsequently, protein IgG was immobilized on the chip surface, covering a wide concentration range of 1 ng/mL to 100 µg/mL. Following each binding step, a thorough rinsing with PBS was performed to eliminate any unbound proteins from the chip surface. Fig. 5A displays the diffraction field intensity values calculated for different IgG concentrations (blue squares) along with protein A/G (green square). In the figure, the squares represent the mean values of three independent experiments, while the error bars indicate double the standard deviation. As expected, increasing the IgG concentration resulted in a shift of the transmission resonance towards longer wavelengths, leading better overlap with the light source. Consequently, the diffraction field intensity values gradually increased with protein concentration, reaching saturation at high IgG concentrations (e.g., 50 µg/mL) due to surface saturation with the targeted analytes. When zooming in on a very small concentration range of IgG, the diffraction intensity values associated with protein A/G (green square) and IgG concentrations (blue squares) from 1 ng/mL to 4 ng/mL overlapped. On the other hand, the intensity associated with 5 ng/mL protein IgG could be reliably differentiated from the others. Thus, the experimental determination of the system's LOD was 5 ng/mL (highlighted in gray in the figure).

The limit-of-detection of the biosensor system depends on the optical and sensitivity properties of the plasmonic chip, as well as the hardware settings such as the LED source and the CMOS camera. By employing different bulk solutions with refractive indices, for example, DI-water ($n = 1.33$), acetone ($n = 1.35$), ethanol ($n = 1.36$), and isopropanol ($n = 1.37$), we determined the refractive index sensitivity of the plasmonic chip as $S = \Delta\lambda/\Delta n = 658.27$ nm/RIU (RIU: refractive index unit) [26]. Supporting a transmission resonance with a linewidth of 40.58 nm, the plasmonic chip yields a figure-of-merit, FOM $= S/\text{Linewidth} = 16.22$ [27]. In addition to the sensitivity parameters, the light source and the CMOS camera parameters have an effect on the variation between the diffraction field intensities. For example, the LED source response has a full-width half-maximum of FWHM $= 27.6$ nm, while the quantum efficiency of the camera slightly varies with wavelength within the spectral region of interest. Moreover, during the real-time binding of analytes, the transmission amplitude slightly decreases, e.g., ~5% for the case of surface saturation with protein IgG. Therefore, employing plasmonic chips that exhibit sharper transmission resonances and support larger refractive index sensitivities, along with using light sources with narrower responses, could yield high-contrast diffraction field images. This would result in better refractive index

sensitivities for plasmonic biosensing approaches based on an imaging-based read-out scheme.

In addition to the preceding information, it is important to note that our low-cost manufacturing technique necessitates the application of a thin layer of liquid PDMS on the surface of PDMS layer. Consequently, the feasibility of producing multiple channels within the space required to align with the active area of the CMOS imager was constrained. To enhance the sensing capabilities of our portable platform, further investigation into advanced manufacturing techniques could be followed. Specifically, efforts could be directed towards realizing a sensor channel in conjunction with a control channel. This improvement has the potential to significantly enhance the detection limit by effectively mitigating the influence of mechanical or optical fluctuations, while also enabling the subtraction of background noise. By incorporating such developments, our sensor system could achieve higher precision and sensitivity in real-time measurements, contributing to the overall robustness and reliability of the platform.

7. Portable platform defines molecular binding kinetics

As demonstrated in our previous work, our handheld platform has the potential to detect a variety of analytes for multiplexed biosensing or ensure test reliability through high-throughput detection of the same analyte [18]. By incorporating microfluidics and monitoring multiple sensor locations on a single plasmonic chip, our technology also enables high-throughput and multiplexed biosensing for real-time binding kinetic applications [20]. In this study, we conducted a proof-of-principle experiment to demonstrate our platform's capability in elucidating the binding kinetics of biomolecules. Furthermore, in sharp contrast to our previous studies,[18–20] which primarily focused on developing cost-effective instrumentation, we have diligently implemented measures to curtail expenses related to manufacturing, fabrication, and sample preparation techniques. As a result, the core essence of this article revolves around our unwavering dedication to determining the binding parameters associated with the analytes of interest, mirroring the approach adopted by their commercial SPR device counterparts. Consequently, given our adherence to an imaging-based technique, our primary emphasis lies on investigating these parameters from a singular location, much akin to the classical spectrometer-based methodologies employed by commercial SPR systems. The pursuit of multiplexing or throughput capabilities, though alluring, remains beyond the immediate scope of this work.
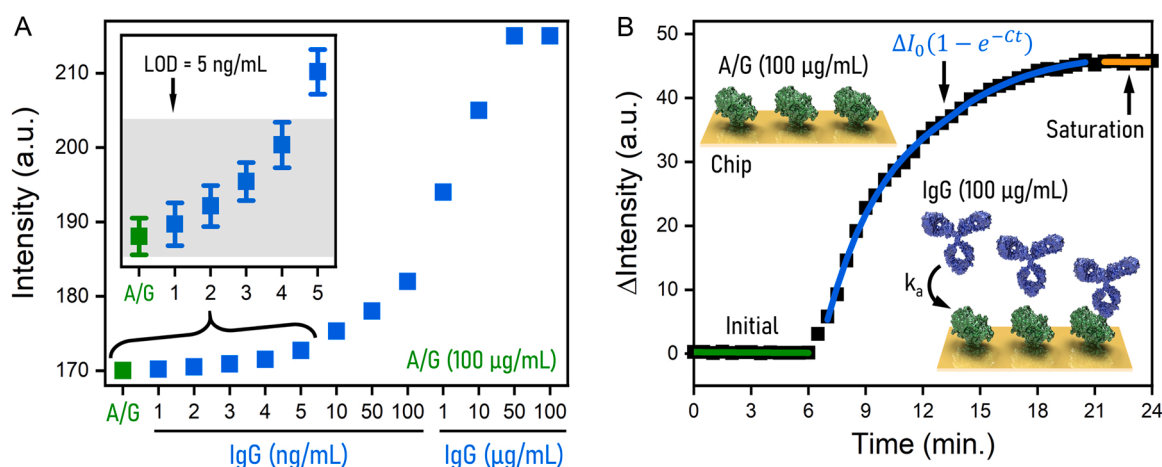
Fig. 5. (A) Diffraction field intensity values for different IgG concentrations (blue squares) compared to the control (A/G, green square). Each square represents the average intensity value derived from three independent experiments, with error bars indicating double the standard deviation. The protein IgG concentration ranges from 1 ng/mL to 100 µg/mL. The figure inset zooms in on the IgG concentration range between 1 ng/mL and 5 ng/mL. The limit of detection (LOD) of the plasmonic platform is highlighted in gray. (B) Change in diffraction field intensity over a 25-minute period. Green: Protein A/G-coated chip, Blue: Response change of the chip after infusion of protein IgG solution, Orange: Surface saturation with protein IgG.

Specifically, we investigated the interaction between protein A/G and IgG to provide a clear demonstration. To achieve this, we flowed a target solution containing protein IgG over the nanohole surface functionalized with A/G, resulting in the formation of the IgG-A/G protein complex. The binding process between these two proteins is governed by the association constant, k_a. The kinetics of the molecular interaction between protein A/G and IgG over time could be modeled according to reference [28].

$$\frac{d[IgG - A/G]}{dt} = k_a[IgG][A/G] - k_d[IgG - A/G]$$

where k_d is the disassociation constant for protein A/G and IgG. Here, the rate of change in the diffraction field intensity is associated with the formation of the IgG-A/G protein complex. Specifically, the integral of the time-dependent molecular interaction kinetics provides insights into the association – disassociation rate relationship.

$$\Delta I(t) = k_a[IgG]\Delta I_{max}\frac{1 - e^{(-k_a[IgG]+k_d)t}}{k_a[IgG] + k_d}$$

where ΔI_{max} is the maximum diffraction field intensity change associated with the nanohole surface saturated with protein IgG, and $\Delta I(t)$ is the change in the intensity at time t. Arranging the terms yields,

$$\Delta I(t) = \Delta I_0\left(1 - e^{-Ct}\right)$$
$$C = k_a[IgG] - k_d$$
$$\Delta I_0 = \frac{k_a[IgG]\Delta I_{max}}{k_a[IgG] + k_d}$$

where [IgG] is the concentration of protein IgG.

Fig. 5B depicts the variation in the diffraction field intensity as protein IgG is passed over a surface coated with protein A/G over a duration of 25 min. The initial 6 min represent the chip's initial response when coated with 100 μg/mL protein A/G, demonstrating its consistent behavior (green curve). Here, the surface was initially functionalized with a high concentration of protein A/G to saturate the biosensing zone with the capturing agent. This ensures the effective capture of the analytes by the ligand on the surface, even at very low concentrations. Subsequently, the attachment of protein IgG for 15 min resulted in an exponential increase in the diffraction field intensity (blue curve). Once a high protein concentration, e.g., 100 μg/mL, was reached, the sensing surface became saturated, and no further changes in intensity were observed (orange curve). The intensity value associated with the situation of surface saturations is used to determine ΔI_{max}. Additionally, by employing our exponential model, we computed values for C and ΔI_0. Using the known values of ΔI_{max}, C and ΔI_0, we calculated the association and dissociation constants as: $k_a = 3.41 \times 10^5(1/Ms)$ and $k_d = 5.28 \times 10^{-7}(1/s)$. These calculated values closely align with the literature values of $k_a = 3.11 \times 10^5(1/Ms)$ and $k_d < 10^{-6}(1/s)$ for protein IgG (molecular weight of 160 kDa) [29].

8. Software module

Fig. 6A shows the main panel of the Python-based Software Module, which is composed of a graphical user interface (GUI) and an image-processing algorithm. GUI enables to control the hardware components of the Imaging and Microfluidic modules of the portable plasmonic platform. GUI connects to the CMOS camera via the camera DLL file, and allows the operator to adjust parameters, e.g., exposure time and gain (Camera Settings panel). Operator could also capture images and save the frames. Pump Modes panel enables to adjust the flow rate of the piezoelectric pump in two different format, e.g., flow rate, or infuse duration and total solution volume, using the linear relationship between flow rate and the applied potential as explained before. Piezoelectric pumps need to be calibrated for accurate flow rates under the solutions used in the binding tests. For this purpose, Pump Settings panel has a Pump Calibration sub-panel that enables to run the piezoelectric pumps for up to 10 potential values between 0 and 4.5 V under the calibration solutions with the user given density values. For an accurate flow rate calculation, minimum 5 potential values were driven, and the calibration reliability was ensured with up to three times test repetition for each value. Calculation of the binding constants is performed in Biosensor Settings panel that uses the real-time binding equation based on the diffraction field intensities and the user given parameters, e.g., molarity (M = mol/L), or concentration (μg/mL) and molecular weight (kDa). This panel also allows the operator to observe the diffraction field images in real-time. The operator can select a region on the image of the plasmonic chip using the SENSOR icon. Subsequently, the software
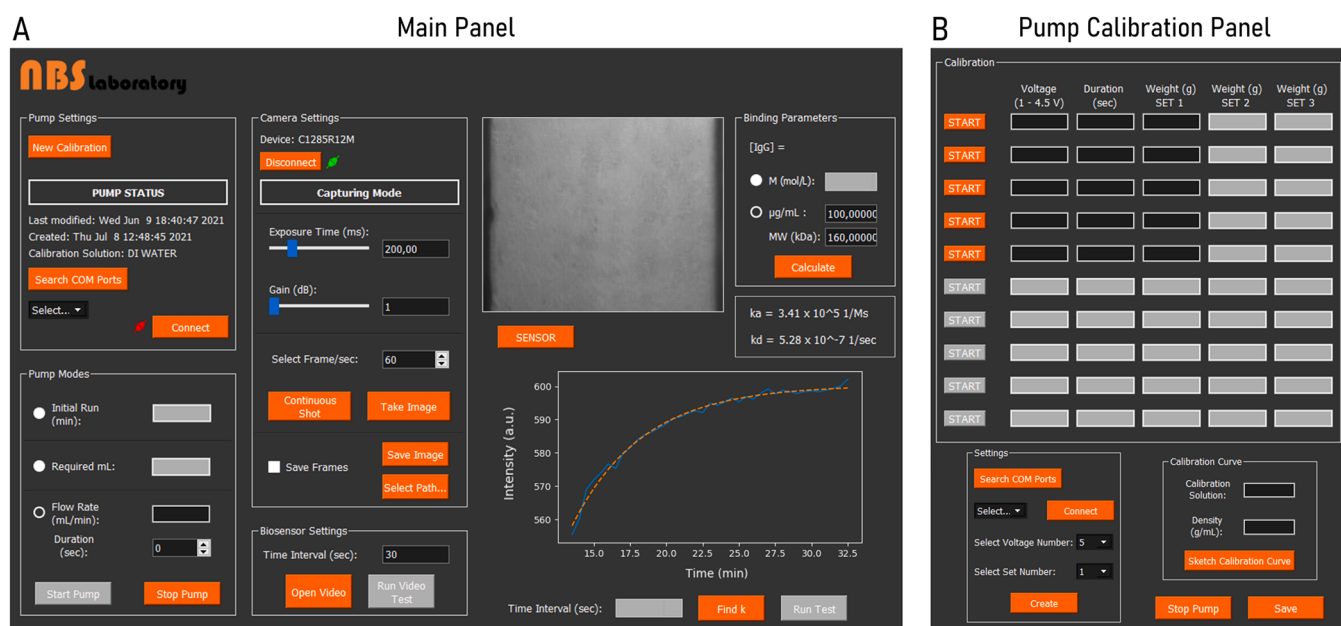
Fig. 6. (A) Main panel of the graphical user interface (GUI) enabling hardware control and binding constant calculations. (B) Calibration sub-panel for piezo pump calibration with user-provided solutions.

calculates the average diffraction field intensity within this selected region for each frame, and plots the intensity in real-time, considering the time interval chosen by the operator between each frame. Finally, the operator calculates the association and disassociation constants, k_a (1/Ms) and k_d (1/s), using the real-time exponential relationship between diffraction field intensity and analyte concentration. This software possesses the capability to interface with various hardware components through their DLL files or a micro-controller, such as Arduino. Consequently, it can be easily adapted to work with different cameras or pumps.

9. Discussion

The presented handheld technology possesses the attributes of portability, cost-effectiveness (~$500), and rapidity, rendering it a favorable option for scenarios where the paramount factors entail mobility, economic efficiency, and swift processing. One such illustrative application of this technology lies in point-of-care diagnostics or field settings, where its attributes are highly advantageous. On the other hand, SPR (Surface Plasmon Resonance) represents an expensive benchtop technology (typically >$100,000 and 10–20 kg) distinguished by a broader dynamic range with heightened specificity and sensitivity (10–100 pg/mL) [30]. Thus, it emerges as a commendable choice for contexts demanding extensive dynamic coverage and elevated levels of selectivity. Notably, its employment finds pertinence in research applications, wherein precision and accuracy are pivotal, as well as in drug development endeavors, where exacting detection and analysis are imperative. Furthermore, our handheld technology is easy-to-use, while SPR requires trained professionals.

The indented applications of our technology offer a range of valuable capabilities. Firstly, it enables label-free identification of biomolecular interactions, allowing the detection and quantification of biomolecules without the use of labeling agents. This feature proves particularly beneficial in clinical diagnostics and environmental monitoring where labels may be undesirable due to potential interference or safety concerns. Another crucial application is the real-time measurement of binding kinetics of biomolecules. By assessing the rate at which biomolecules bind to each other, researchers and scientists gain valuable insights into the underlying mechanisms of interactions. This information could lead to the development of novel therapeutic drugs and enhance our understanding of biological processes. Furthermore, the platform's portability and cost-effectiveness contribute to its versatility. It becomes well-suited for various settings, including clinical laboratories, research facilities, and even on-site field use. This portability facilitates convenient and widespread access to binding kinetic measurement capabilities, democratizing the technology's use and impact.

As for potential users, clinicians stand to benefit significantly from our handheld binding kinetic measurement system. It empowers them to diagnose diseases more accurately and monitor treatment effectiveness, leading to improved patient outcomes and personalized medical interventions. Likewise, researchers could find great value in the technology, as it opens up new avenues for studying intricate biomolecular interactions. By elucidating the binding kinetics of molecules, researchers could advance their understanding of biological processes and develop innovative therapeutic approaches. Moreover, environmental scientists could utilize this system to monitor pollutant levels in the environment effectively. Its ease of use and real-time capabilities make it a valuable tool for assessing and addressing environmental challenges, contributing to more sustainable practices. Beyond the specified users, the system's applications extend to a diverse range of professionals. Pharmaceutical scientists could harness its potential in drug development, while food safety inspectors could ensure the quality and safety of food products. Even forensic scientists could benefit from this technology in their investigations. Therefore, our handheld binding kinetic measurement system presents a versatile and impactful tool with widespread applications. Its label-free identification, real-time kinetic measurement, portability, and cost-effectiveness cater to the needs of various sectors, revolutionizing biomolecular research, diagnostics, and environmental monitoring across diverse fields of expertise.

10. Conclusions

In conclusion, we have presented an optofluidic biosensor platform capable of determining the binding parameters of biomolecules. Leveraging the unique optical properties of plasmonic nanohole arrays, our platform provides accurate biosensing data at a low-cost infrastructure. The nanohole arrays are fabricated using a high-throughput, low-cost, and wafer-scale method, resulting in high-quality and uniform apertures across a wide area. With the integration of a compact piezo pump system, we ensure precise and targeted delivery of analytes through a cost-effective microfluidic chamber. Real-time monitoring of biomolecular interactions is achieved using an inexpensive CMOS imager to record diffraction field images. Our platform exhibits a limit-of-detection (LOD) as low as 5 ng/mL for label-free detection of protein IgG. By analyzing the real-time diffraction field images, we could successfully determine the association and disassociation constants for protein A/G and IgG binding. Furthermore, we have developed a software that allows to control the hardware components of the optofluidic platform and includes an algorithm to process diffraction field images, enabling the extraction of binding parameters. With its remarkable capability to ascertain real-time interactions between analytes and ligands, our deployable handheld optofluidic technology holds immense potential for unraveling the intricate binding kinetics between diverse biological and chemical molecules across different fields of application.

CRediT authorship contribution statement

Sena Yaman: Conceptualization, Investigation, Formal analysis, Data curation, Funding acquisition, Writing – original draft. **Meryem Beyza Avci**: Software, Data curation, Writing – original draft. **Fatma Kurul**: Formal analysis, Investigation, Data curation, Writing – original draft. **Seda Nur Topkaya**: Conceptualization, Investigation, Data curation, Writing – original draft. **Arif E. Cetin**: Conceptualization, Investigation, Formal analysis, Data curation, Supervision, Funding acquisition, Writing – original draft, Writing – review & editing.

Declaration of Competing Interest

The authors declare that they have no known competing financial interests or personal relationships that could have appeared to influence the work reported in this paper.

Data availability

Data will be made available on request.

References

[1] H. Altug, S.H. Oh, S.A. Maier, J. Homola, Advances and applications of nanophotonic biosensors, Nat. Nanotechnol. 17 (2022) 5–16, https://doi.org/10.1038/s41565-021-01045-5.

[2] C. Wang, J.J. Morrissey, E.D. Kharasch, S. Singamaneni, Plasmonic Biosensors in Resource-limited Settings, in: Adv. Photonics 2017 (IPR, NOMA, Sensors, Networks, SPPCom, PS), OSA, Washington, D.C., 2017: p. SeTu1E.6. https://doi.org/10.1364/SENSORS.2017.SeTu1E.6.

[3] C. Chen, J. Wang, Optical biosensors: an exhaustive and comprehensive review, Analyst 145 (2020) 1605–1628, https://doi.org/10.1039/c9an01998g.

[4] H. Qu, C. Fan, M. Chen, X. Zhang, Q. Yan, Y. Wang, S. Zhang, Z. Gong, L. Shi, X. Li, Q. Liao, B. Xiang, M. Zhou, C. Guo, G. Li, Z. Zeng, X. Wu, W. Xiong, Recent advances of fluorescent biosensors based on cyclic signal amplification technology in biomedical detection, J. Nanobiotechnol. 19 (2021), 403, https://doi.org/10.1186/s12951-021-01149-z.

[5] A. Camarca, A. Varriale, A. Capo, A. Pennacchio, A. Calabrese, C. Giannattasio, C. M. Almuzara, S. D'auria, M. Staiano, Emergent biosensing technologies based on fluorescence spectroscopy and surface plasmon resonance, Sensors 21 (2021) 1–35, https://doi.org/10.3390/s21030906.

[6] V.R. Samuel, K.J. Rao, A review on label free biosensors, Biosens. Bioelectron. X. 11 (2022), 100216, https://doi.org/10.1016/j.biosx.2022.100216.

[7] G. Nava, G. Zanchetta, F. Giavazzi, M. Buscaglia, Label-free optical biosensors in the pandemic era, Nanophotonics 11 (2022) 4159–4181, https://doi.org/10.1515/nanoph-2022-0354.

[8] M.A. Butt, S.N. Khonina, N.L. Kazanskiy, Recent advances in photonic crystal optical devices: a review, Opt. Laser Technol. 142 (2021), 107265, https://doi.org/10.1016/j.optlastec.2021.107265.

[9] K.J. Vahala Optical microcavities, (2005) Eur. Quantum Electron Conf. EQEC 05 2005 2005 352 doi: 10.1109/EQEC.2005.1567517.

[10] Q. Wang, Z.-H. Ren, W.-M. Zhao, L. Wang, X. Yan, A. Zhu, F. Qiu, K.-K. Zhang, Research advances on surface plasmon resonance biosensors, Nanoscale 14 (2022) 564–591, https://doi.org/10.1039/D1NR05400G.

[11] A. Minopoli, A. Acunzo, B. Della Ventura, R. Velotta, Nanostructured surfaces as plasmonic biosensors: a review, Adv. Mater. Interfaces 9 (2022), 2101133, https://doi.org/10.1002/admi.202101133.

[12] V.G. Kravets, A.V. Kabashin, W.L. Barnes, A.N. Grigorenko, Plasmonic surface lattice resonances: a review of properties and applications, Chem. Rev. 118 (2018) 5912–5951, https://doi.org/10.1021/acs.chemrev.8b00243.

[13] C. Jin, Z. Wu, J.H. Molinski, J. Zhou, Y. Ren, J.X.J. Zhang, Plasmonic nanosensors for point-of-care biomarker detection, Mater. Today Bio. 14 (2022), 100263, https://doi.org/10.1016/j.mtbio.2022.100263.

[14] S.K. Gahlaut, A. Pathak, B.D. Gupta, Recent advances in silver nanostructured substrates for plasmonic sensors, Biosensors 12 (2022) 713, https://doi.org/10.3390/bios12090713.

[15] E. Mauriz, L. Lechuga, Plasmonic biosensors for single-molecule biomedical analysis, Biosensors 11 (2021) 123, https://doi.org/10.3390/bios11040123.

[16] J.F. Masson, Portable and field-deployed surface plasmon resonance and plasmonic sensors, Analyst 145 (2020) 3776–3800, https://doi.org/10.1039/d0an00316f.

[17] M.E. Hamza, M.A. Othman, M.A. Swillam, Plasmonic biosensors: review, Biology 11 (2022) 621, https://doi.org/10.3390/biology11050621.

[18] A.E. Cetin, A.F. Coskun, B.C. Galarreta, M. Huang, D. Herman, A. Ozcan, H. Altug, Handheld high-throughput plasmonic biosensor using computational on-chip imaging, Light Sci. Appl. 3 (2014), https://doi.org/10.1038/lsa.2014.3.

[19] A.E. Cetin, Z.A. Kocer, S.N. Topkaya, Z.A. Yazici, Handheld plasmonic biosensor for virus detection in field-settings, Sens. Actuators B Chem. 344 (2021), 130301, https://doi.org/10.1016/j.snb.2021.130301.

[20] A.F. Coskun, A.E. Cetin, B.C. Galarreta, D.A. Alvarez, H. Altug, A. Ozcan, Lensfree optofluidic plasmonic sensor for real-time and label-free monitoring of molecular binding events over a wide field-of-view, Sci. Rep. 4 (1) (2014) 7, https://doi.org/10.1038/srep06789.

[21] I.M. White, X. Fan, On the performance quantification of resonant refractive index sensors, Opt. Express 16 (2008) 1020, https://doi.org/10.1364/OE.16.001020.

[22] A.E. Cetin, D. Etezadi, B.C. Galarreta, M.P. Busson, Y. Eksioglu, H. Altug, Plasmonic nanohole arrays on a robust hybrid substrate for highly sensitive label-free biosensing, ACS Photonics 2 (2015) 1167–1174, https://doi.org/10.1021/acsphotonics.5b00242.

[23] A.H. Johnstone, CRC Handbook of chemistry and physics, J. Chem. Technol. Biotechnol. 50 (2007) 294–295, https://doi.org/10.1002/jctb.280500215.

[24] A.E. Cetin, H. Altug, Fano resonant ring/disk plasmonic nanocavities on conducting substrates for advanced biosensing, ACS Nano 6 (2012), https://doi.org/10.1021/nn303643w.

[25] A.E. Cetin, S.N. Topkaya, O. Yalcin-Ozuysal, A. Khademhosseini, Refractive index sensing for measuring single cell growth, ACS Nano (2021), https://doi.org/10.1021/acsnano.1c04031.

[26] A.A. Yanik, A.E. Cetin, M. Huang, A. Artar, S.H. Mousavi, A. Khanikaev, J. H. Connor, G. Shvets, H. Altug, Seeing protein monolayers with naked eye through plasmonic Fano resonances, Proc. Natl. Acad. Sci. 108 (2011) 11784–11789, https://doi.org/10.1073/pnas.1101910108.

[27] P. Offermans, M.C. Schaafsma, S.R.K. Rodriguez, Y. Zhang, M. Crego-Calama, S. H. Brongersma, J. Gómez Rivas, Universal scaling of the figure of merit of plasmonic sensors, ACS Nano 5 (2011) 5151–5157, https://doi.org/10.1021/nn201227b.

[28] K. Saha, F. Bender, E. Gizeli, Comparative study of IgG binding to proteins G and A: nonequilibrium kinetic and binding constant determination with the acoustic waveguide device, Anal. Chem. 75 (2003) 835–842, https://doi.org/10.1021/ac0204911.

[29] V. Bronner, M. Tabul, T. Bravman, Rapid screening and selection of optimal antibody capturing agents using the ProteOn XPR36 protein interaction array system, Bio-Rad. Tech. Note (2006) 5820.

[30] H. Nguyen, J. Park, S. Kang, M. Kim, Surface plasmon resonance: a versatile technique for biosensor applications, Sensors 15 (2015) 10481–10510, https://doi.org/10.3390/s150510481.

Sena Yaman completed her Ph.D. in 2020 at the Department of Bioengineering, Izmir Institute of Technology. She is currently a Postdoctoral Researcher at the Department of Radiology, Stanford University. In 2021, she worked as a Postdoctoral Researcher at the Izmir Biomedicine and Genome Center. Her research interests mainly focus on bioassay development, bead-based biosensing, magnetic levitation, and cell separation.

Meryem Beyza Avci received her B.S. degree from Izmir University of Economics in 2021. She is currently a master's student in the Department of Electrical and Electronics Engineering at Izmir University of Economics. Her research interests mainly focus on medical image processing, intelligent systems, and microscopy.

Fatma Kurul received her B.S. degree from Pamukkale University in 2020. She is currently pursuing a master's degree at the Department of Biomedicine and Health Technologies at Dokuz Eylul University, Izmir Biomedicine and Genome Institute. In 2022, she served as a Visiting Research Student at the Nano- and Microrobotics Lab at the Technical University of Munich. Her research interests include the development of point-of-care devices based on electrochemical and optical techniques for biomedical applications.

Seda Nur Topkaya received her Ph.D. in 2013 from the Faculty of Pharmacy at Ege University, Turkey, in the field of Analytical Chemistry. Currently, she is a Professor and the head of the Department of Analytical Chemistry at Izmir Katip Celebi University. Her research interests include electrochemistry, biosensor systems, drug-DNA interactions, and electrochemical-based DNA biosensors. She has published 36 papers in journals indexed by SCI, serves as a reviewer, and is an editorial board member for various international journals. Dr. Topkaya has conducted research at several institutions around the world, including the Academy of Science of the Czech Republic in Brno, Czech Republic, Joseph Fourier University in Grenoble, France, Harvard Medical School-MIT in Cambridge, U.S.A., and Max Planck Institute for the Science of Light in Erlangen, Germany.

Arif E. Cetin is a Group Leader in Izmir Biomedicine and Genome Center (IBG), locating in Izmir, Turkey. Dr. Cetin received his BS degree in Electrical and Electronics Engineering and MS degree in Electrical and Computer Engineering both from Koc University, Istanbul, Turkey. He received his PhD degree in Electrical Engineering from Boston University, Boston, MA, USA. He worked as a postdoctoral associate at EPFL (Swiss Federal School in Lausanne), Switzerland in 2013–2014, as a postdoctoral fellow at Massachusetts Institute of Technology (MIT), Cambridge, MA, USA in 2014–2016, and as a research scientist at Omniome Inc., San Diego, CA, USA in 2016–2018. Dr. Cetin pursues research on optical nano-biosensors integrated with microfluidic platforms for ultrasensitive label-free biodetection. He developed hand-held biosensors for high-throughput and multiplexed biosensing sensors for growth rate cytometry to determine therapeutic susceptibility of cancer cells for personalized drug therapy. Recently, he also developed a unique label-free technique for high-throughput DNA sequencing.